Microendoscopy for periodic intravital end-to-end tumor imaging of cancer cells

Goto, Toshiyuki ; Nakano, Masayuki ; Danno, Sally ; Ueda, Chie ; Sakaue-Sawano, Asako ; Miyawaki, Atsushi ; Wrabel, Anna ; Nakahara,…

(Citation)
Cell Reports Methods,5(6):101056

(Issue Date)
2025-06-04

(Resource Type)
journal article

(Version)
Version of Record

Cell Reports
Methods

Article

Microendoscopy for periodic intravital end-to-end tumor imaging of cancer cells

Graphical abstract

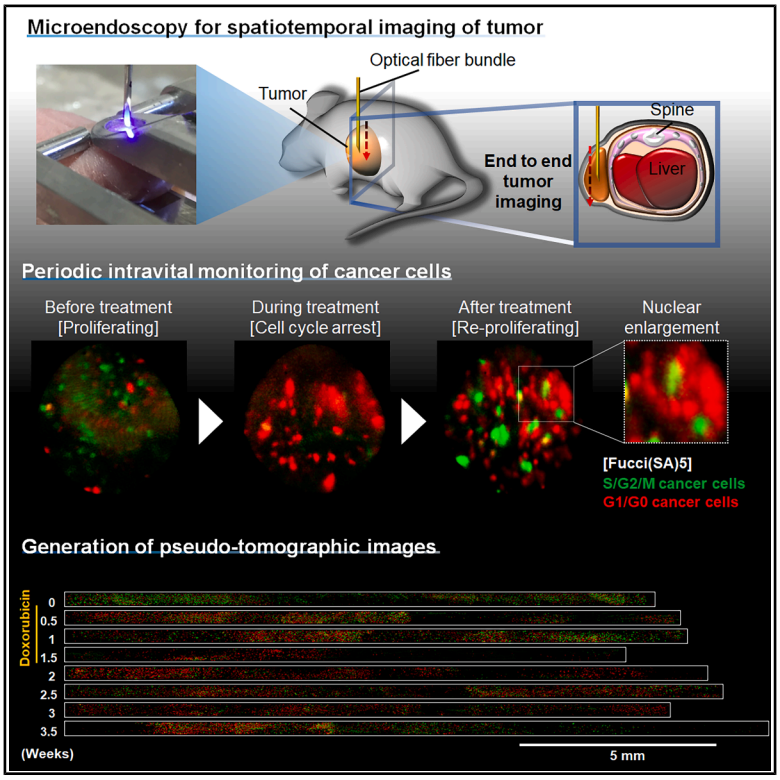

Highlights

- We present a microendoscopy method for intravital imaging of cancer cells
- We demonstrate live imaging of Fucci-reporter cancer cells in tumor-bearing mice
- Proliferation and nuclear enlargement of the cells are spatiotemporally visualized
- We report complex temporal changes in these cell states in response to anticancer drugs

Authors

Toshiyuki Goto, Masayuki Nakano, Sally Danno, ..., Kei Mizuno, Yosky Kataoka, Kazuo Funabiki

Correspondence

kataokay@person.kobe-u.ac.jp (Y.K.), funabiki@ent.kuhp.kyoto-u.ac.jp (K.F.)

In brief

Goto et al. report a microendoscopic technique enabling intravital, end-to-end tumor imaging at cellular-level resolution in tumor-bearing mice. They demonstrate proliferative activity and nuclear enlargement of cancer cells in response to tumor growth and/or anticancer drugs for several weeks. This technique can accelerate innovation in cancer biology and therapeutics.

Goto et al., 2025, Cell Reports Methods *5*, 101056
June 16, 2025
https://doi.org/10.1016/j.crmeth.2025.101056

CellPress

Please cite this article in press as: Goto et al., Microendoscopy for periodic intravital end-to-end tumor imaging of cancer cells, Cell Reports Methods (2025), https://doi.org/10.1016/j.crmeth.2025.101056

Cell Reports Methods

CellPress
OPEN ACCESS

Article

Microendoscopy for periodic intravital end-to-end tumor imaging of cancer cells

Toshiyuki Goto,[1,2,3] Masayuki Nakano,[1] Sally Danno,[1,3] Chie Ueda,[1,3] Asako Sakaue-Sawano,[4,5] Atsushi Miyawaki,[4,5] Anna Wrabel,[1] Ichiro Nakahara,[1] Takahito Nishikata,[2] Akira Mizoguchi,[1,6] Yasuhisa Tamura,[1,3] Kei Mizuno,[1,3] Yosky Kataoka,[1,3,7,9,*] and Kazuo Funabiki[1,8,*]

[1]RIKEN Center for Biosystems Dynamics Research, Kobe, Hyogo 650-0047, Japan
[2]Frontiers of Innovative Research in Science and Technology (FIRST), Konan University, Kobe, Hyogo 650-0047, Japan
[3]Graduate School of Science, Technology and Innovation, Kobe University, Kobe, Hyogo 650-0047, Japan
[4]RIKEN Center for Brain Science, Wako, Saitama 351-0198, Japan
[5]Biotechnological Optics Research Team, RIKEN Center for Advanced Photonics, Wako, Saitama 351-0198, Japan
[6]Graduate School of Medicine, Mie University, Tsu, Mie 514-8507, Japan
[7]RIKEN-JEOL Collaboration Center, RIKEN Baton Zone Program, Kobe, Hyogo 650-0047, Japan
[8]Foundation for Biomedical Research and Innovation, Kobe, Hyogo 650-0047, Japan
[9]Lead contact
*Correspondence: kataokay@person.kobe-u.ac.jp (Y.K.), funabiki@ent.kuhp.kyoto-u.ac.jp (K.F.)
https://doi.org/10.1016/j.crmeth.2025.101056

MOTIVATION The heterogeneity in cancer cell behaviors in tumor is considered the main reason for the difficulty in achieving complete remission. To determine the efficacy of anticancer treatments, the behavior of cancer cells should be investigated at a cellular resolution in all the different micro- and macroenvironments within each tumor. However, current intravital imaging methods do not realize that. Thus, we developed an optical-fiber-bundle-based microendoscopy with a fluorescent ubiquitination-based cell- cycle indicator (Fucci) system to achieve the intravital, periodic, and multicolor end-to-end tumor imaging of the proliferative activity of cancer cells at a cellular-level resolution.

SUMMARY

The spatiotemporal heterogeneity in intratumor proliferative behavior of cancer cells deeply affects tumor environment characteristics and the efficacy of anticancer treatments. Thus, intravital imaging with unlimited imaging depth and cellular-level resolution is greatly desired. We developed an optical-fiber-bundle-based microendoscope with a genetically encoded fluorescent ubiquitination-based cell-cycle indicator (Fucci) system to achieve the intravital, periodic, and multicolor end-to-end imaging of the proliferative activity of cancer cells at a cellular-level resolution. This technique enabled the periodic visualization of spatiotemporal cellular responses, including cell-cycle arrest and resumption, and nuclear enlargement following the administration of anticancer drugs in living mice. It was suggested that proliferating cell ratio and nuclear enlargement in cancer cells at the surface region of tumor characterized by abundant vascular invasion contribute to aggressive tumor regrowth after chemotherapy. The application of this technique can accelerate innovation in cancer biology and therapeutics.

INTRODUCTION

Tumor progression is influenced by the relationship between the proliferation rate and cell death.[1] However, such tumor cell behaviors are not homogeneous in tumor micro- and macroenvironments.[2–4] Tumor cells show different proliferation activities in the surface, core, and avascular regions of tumors.[5,6] The heterogeneity in tumor cell behavior is considered the main reason for the difficulty in achieving complete remission.[7,8] To determine the efficacy of anticancer treatments, the behavior of cancer cells should be investigated at a cellular resolution in all the different environments within each tumor. Imaging techniques are indispensable for understanding tumor biology, predicting clinical prognosis, and evaluating treatments. Currently, *in vivo* imaging systems such as computed tomography (CT), positron emission tomography, near-infrared fluorescence imaging, optical coherence tomography, photoacoustic imaging, ultrasound imaging, and magnetic resonance imaging are widely used to investigate tumor progression in tumor-bearing animals. In recent technical advances, the spatial resolution has greatly improved, such as photon-counting CT,[9] second near-infrared imaging,[10] super-resolution ultrasound imaging,[11,12] and ultrahigh-field magnetic

Please cite this article in press as: Goto et al., Microendoscopy for periodic intravital end-to-end tumor imaging of cancer cells, Cell Reports Methods (2025), https://doi.org/10.1016/j.crmeth.2025.101056

resonance imaging.[13,14] However, currently these imaging techniques do not allow for imaging *in vivo* at a cellular resolution. Microscopic evaluation of tumors has long been performed after excision, fixation, and staining of the fixed tissue.[15] Accordingly, a considerable number of animals are required to examine the cell dynamics or efficacy of anticancer agents using histological methods. Although multiphoton microscopy has been used for intravital imaging of tumor invasion and cancer cell behavior[16] and to determine immune responses[17] at a cellular resolution in living animals, its application is limited to the subsurface of tumors (depth less than 1.0 mm). The three-photon fluorescence microscope is a recent advance in multiphoton microscopy; it has an imaging depth greater than 1 mm in brain imaging.[18] Light-sheet microscopy combined with second near-infrared or three-photon fluorescence microscopy has also archived the imaging depth of more than 1 mm.[19,20] However, even with these microscopies, it is difficult to visualize deeper tissue structures reaching more than several millimeters or 1 cm. Furthermore, periodic observations are difficult owing to their invasiveness. Tumor progression and anticancer therapies are known to vary the tumor environments, including spatiotemporal cell population and behavior not only in cancer cells but in immune cells. Thus, a new intravital imaging method enabling repeated evaluations of cell behavior at cellular resolution in the end-to-end tumor is desired.

Fiber-bundle-based microendoscopes allow minimally invasive and high-resolution imaging in tissues, even at greater depths.[21] Such a microendoscope was previously used to visualize neuronal activity[21–23] and blood flow[24] in the mouse brain. These imaging methods are performed at single or multiple imaging points at the desired tissue depth. Microendoscopy is likely used to understand spatiotemporal tissue information at a cellular-level resolution in the entire traveling direction of a glass fiber. Herein, we report an improved multicolor microendoscopic technique for application in tumor biology. The technique can provide periodic data on cell behavior at a cellular resolution in different micro- and macroenvironments within entire xenograft tumors for a long period during tumor progression. To visualize the spatiotemporal patterns of cell-cycle dynamics, a genetically encoded fluorescent ubiquitination-based cell-cycle indicator (Fucci) system was introduced into transplanted tumor cells. The Fucci system is suitable for our microendoscopic imaging because the fluorescence emitted from cell nuclei can be recognized at a high spatial resolution and signal/noise ratio.[25,26] Moreover, we succeeded in reconstructing a two-dimensional (2D) pseudo-tomographic image from a microendoscopic imaging video during the travel of an optical fiber within each tumor. This enhanced the recognition of the cell-distribution pattern in the tract of the optical-fiber bundle in the panoramic view. We also performed a spatiotemporal evaluation of anticancer drug efficacy through periodic imaging during the entire examination. Hence, this imaging technique can accelerate innovations in tumor biology and anticancer therapeutics.

RESULTS

Settings and evaluation of fiber-bundle-based microendoscopy for longitudinal imaging of tumors

Microendoscopy with a lens-less optical-fiber bundle (350 μm in diameter) comprising 10,000 optical fibers (each fiber being 2 μm in diameter) was used in this study. The tip of the fiber bundle at the insertion side was processed using a polishing machine to obtain the desired angles and shapes for smooth insertion into the living tissue with minimum invasiveness, depending on the tissue type or application.[21–23,27] In this study, we developed a microendoscope for the longitudinal imaging of tumors by introducing a bamboo spear-shaped tip beveled at 60° (Figure 1A). The spatial resolution of the developed microendoscope was evaluated by observing test fluorescence beads with diameters of 1, 2, 5, and 10 μm. Our endoscope clearly detected at least 2-μm beads, providing an adequate resolution for the observation of cell somata and nuclei (Figure 1B). Figure 1C shows an illustration of the insertion of the optical-fiber-based microendoscope in a tumor-bearing mouse. The tip of the optical fiber was inserted into the tumor held with a stereotaxic instrument (Figure 1D). The wound made by the insertion of the optical fiber was tiny and did not show any hemorrhage (Figure 1E). The penetration site was hardly recognized after 2 days. This result indicates that our endoscope can be used for *in vivo* imaging at a resolution comparable to cellular-level resolution with minimal invasiveness.

We then assessed the performance of the developed microendoscope in tumor-bearing mice. Human fibrosarcoma HT1080 cells expressing tFucci(SA)5[25,26,28] (HT1080/Fucci(SA)5) were subcutaneously xenografted into BALB/c nu/nu mice. The cell-cycle state of HT1080/Fucci(SA)5 cells was indicated through the emission of red (G1/G0 phase) or green (S/G2/M phase) fluorescence. Microendoscopy provided a clear dynamic image of fluorescence signals. The fluorescence pattern of the cell population varied during the insertion of the optical fiber from one surface to the other through the core of the tumor, suggesting heterogeneity in the tumor environment. An example of *in vivo* imaging is shown in Video S1. Because the fiber proceeded at 0.069 mm/s, the inserted fiber was speculated to reach the opposite surface of a 1-cm-diameter-tumor in approximately 2.5 min. Using the beveled face of the optical-fiber tip, objective structures were extended in the direction of cell travel in the endoscopic images depending on the fiber proceeding speed and scanning frame rate (7.5 frames per second [fps] in this study). To compensate for this image distortion, endoscopic images were corrected using confocal microscope images of 30-μm-thick tissue sections of the same tumor, HT1080/Fucci(SA)5, after fixation following endoscopic imaging (Figure 2A). The ratios of the major and minor axes of cell nuclei in the confocal images of the fixed tissue were 1.54 ± 0.06. We calibrated the aspect ratios of nuclei in the compensated endoscopic images to approximately 1.59 ± 0.05 to achieve closer aspect ratios to those in the confocal images. The average cell density in endoscopic images was 28.60 ± 7.67 cells/mm^2, whereas that in the corresponding confocal images of 30-μm-thick sections was 62.3 ± 24.0 cells/mm^2, indicating that the scan depth of our imaging probe was approximately 13.8 μm. A 15-μm-thick optical section of confocal images showed 34.5 ± 17.9 cells/mm^2 (data not shown), comparable to the cell density in endoscopic images. To confirm the correlation of proliferative activity of cancer cells between endoscopic and confocal microscopic images, we compared the spatial patterns of the cell population with Fucci(SA)5 (G1/G0 or S/G2/M cells) using the same tumor.

Please cite this article in press as: Goto et al., Microendoscopy for periodic intravital end-to-end tumor imaging of cancer cells, Cell Reports Methods (2025), https://doi.org/10.1016/j.crmeth.2025.101056

CellPress
OPEN ACCESS

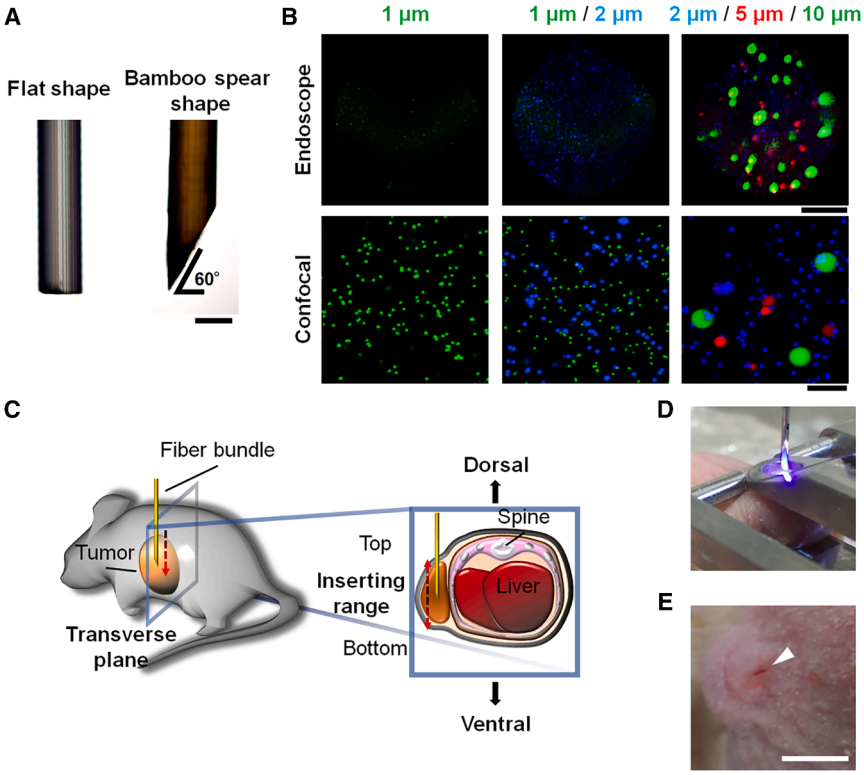

Figure 1. Outline of the fiber-bundle-based microendoscopic imaging system

(A) Microscopic images of polished optical fibers (high-definition image guide [HDIG] fiber) with flat-shaped or bamboo spear-shaped tips. The diameter of an optical fiber is 350 μm. Scale bar, 0.2 mm.

(B) Microendoscopic imaging of multicolor and multisize beads. Fluorescence beads scattered into circles in coagulated 0.8% agarose S. Representative images are shown, in which fluorescent beads with diameters of 1 μm (green, ex: 485 nm), 2 μm (blue, ex: 660 nm), 5 μm (red, ex: 569 nm), or 10 μm (green, ex: 485 nm) are observed using a microendoscope (upper) or confocal microscope (lower). Scale bars, 0.1 mm (endoscope) and 20 μm (confocal).

(C) Schematic of the microendoscopic imaging system for cancer imaging used in this study. The optical fiber longitudinally progressed into the tumor along the dorsoventral axis.

(D) Macroscopic image showing the insertion of an optical fiber into the tumor held with a stereotaxic instrument.

(E) Macroscopic image of the wound made by the insertion of an optical fiber into the tumor. Scale bar, 5 mm.

The endoscopic images successfully demonstrated a spatial pattern of G1/G0 or S/G2/M cell densities similar to that in the confocal images (Figures 2B and 2C). Thus, our endoscopy enabled the rapid acquisition of accurate longitudinal tumor tissue information.

Time-course end-to-end spatiotemporal information of the tumor, including alterations of the nuclear size and cell-cycle phase, was obtained by tracking each cell using the ImageJ plugin (wrMTrck; Figures S1A and Video S2). The S/G2/M cell ratio, referred to as the cell proliferation rate in longitudinal imaging of tumors, was decreased with tumor growth (Figures 2D and 2D′). Conversely, no significant change in the nuclear size in G1/G0 and S/G2/M cells was observed in the tracked cells (Figure 2D′′). We tested whether repetitive fiber insertions affected tumor growth and the spatial pattern of cell proliferation activity by comparing the data on tumor size and S/G2/M cell ratio at 4 weeks after xenograft transplantation between animals that underwent single or repetitive fiber insertions twice a week. We did not detect any significant differences in the S/G2/M cell ratio between the two animal groups (Figures S1B–S1D). These histological analyses after the single-fiber insertion showed that cancer cells exist in high density at the surface region of the tumor, and immune cells infiltrated and accumulated in the necrotic and fibrous core region (Figures S1E and S1F). In contrast, tissue specimens after repetitive fiber insertions also showed similar histological patterns to those after single-fiber insertion (Figures S1E and S1F). These histological findings indicated that the repetitive insertion of the optical fiber in the tumor did not induce an obvious wound response in this study.

In confocal microscopic images at 4 weeks after establishing the xenograft, G1/G0 and necrotic cells exhibited a heterogeneous distribution, including the region of the maximal G1/G0 cell density (Rmax) at the tumor core, whereas S/G2/M cells were dominant at the tumor surface (Figures 2E and S2A). Owing to a bipolarization pattern in histological data, to evaluate spatial cellular information using endoscopy, the tumor surface and center regions in this study were defined at 5% of tumor diameter from bilateral surfaces (top and bottom) and 10% from the center of tumor, respectively. The endoscopic images showed a large number of S/G2/M cells at both surfaces (top and bottom), whereas G1/G0 cells mainly emerged at the center and Rmax regions (Figure 2F). Simultaneous endoscopic imaging of blood vessels with the proliferative activity of cancer cells revealed that vascular density was higher at the surface region of the tumor characterized by a large number of S/G2/M cells compared with that in the central region containing numerous G1/G0 cells (Figures S2C–S2E). The endoscopic image and scatterplot of the individual sizes of nuclei in both G1/G0 and S/G2/M cells obtained using longitudinal endoscopic imaging showed a large number of S/G2/M cells at the surfaces (Figures 2G and 2H). The numbers of G1/G0 and S/G2/M cells at the surface and central regions of the tumor were counted using endoscopy, revealing a greater number of S/G2/M cells around the tumor surface (Figure 2I). In contrast, the numbers of S/G2/M cells at the surface regions in endoscopic imaging were slightly higher than in confocal imaging, but the central region showed no significant difference (Figure S2B). In contrast, no differences were observed in the sizes of nuclei between S/G2/M and G1/G0 cells, both at the surface and center

Please cite this article in press as: Goto et al., Microendoscopy for periodic intravital end-to-end tumor imaging of cancer cells, Cell Reports Methods (2025), https://doi.org/10.1016/j.crmeth.2025.101056

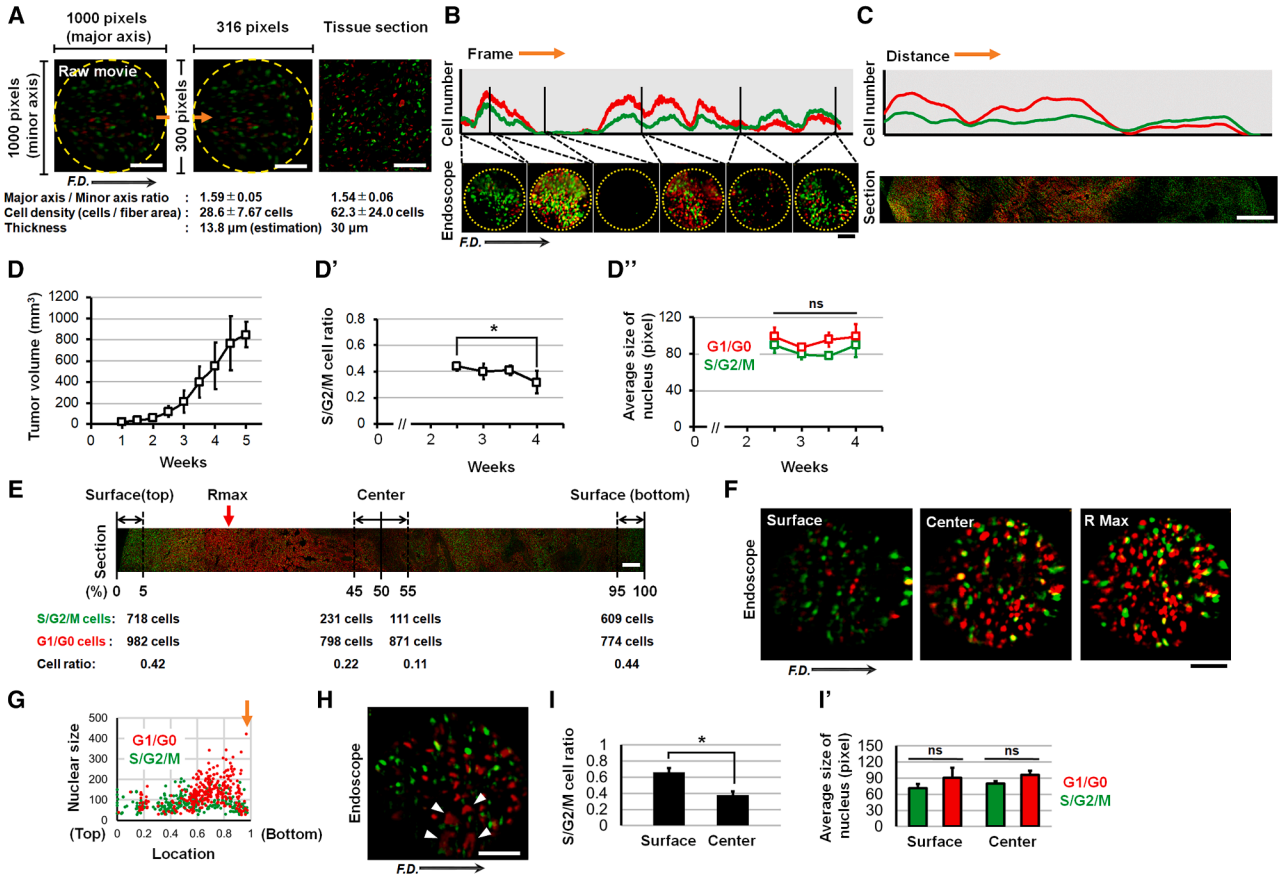

Figure 2. Fiber-bundle-based microendoscopic imaging system enables periodic end-to-end imaging of a longitudinal tumor

(A) Flowchart of image adjustment in a microendoscopic image for equivalency to conventional confocal microscopic images of tissue sections from the fixed tumor. The distortion in microendoscopic images after their resizing was compensated to achieve a comparable ratio between the long and short axes of elliptic fits of cell nuclei to those obtained from confocal microscopic images. The ratios of the major and minor axes, cell density, and thickness in microendoscopic and confocal images are shown (n = 4 tumors). Yellow circles indicate the imaging field of view of the optical fiber. Scale bar, 0.1 mm. Arrow (F.D.) indicates the traveling direction of the optical fiber.

(B) Alterations in the cell number and microendoscopic images of HT1080/Fucci(SA)5 cells in the fixed tumor. Yellow circles indicate the imaging field of view of the optical fiber. The red and green plots indicate the number of G1/G0 and S/G2/M cells in each frame, respectively. Scale bar, 0.1 mm. Arrow (F.D.) indicates the traveling direction of the optical fiber.

(C) Alterations in the cell number and confocal microscopic images of HT1080/Fucci(SA)5 cells in the fixed tumor section around the track of the microendoscope. The red and green graphs indicate the number of G1/G0 and S/G2/M cells, respectively. Scale bar, 1 mm.

(D) BALB/c (nu/nu) nude mice were subcutaneously injected with 1×10^6 HT1080/Fucci(SA)5 cells. Tumor volume was measured twice per week after the injection (week 0). (D′) Endoscopic analysis of periodic alterations in the ratio of S/G2/M cells. (D″) Endoscopic analysis of periodic alterations in the average nuclear size of tracked cells in HT1080/Fucci(SA)5 cancer cell-bearing nude mice. Red and green boxes indicate the number of G1/G0 and S/G2/M cells, respectively. Data are presented as the mean ± SEM, n = 4 mice. *p = 0.085, based on one-way ANOVA followed by the Tukey-Kramer test.

(E) Confocal image of HT1080/Fucci(SA)5 cells in the xenograft tumor in a nude mouse. The numbers of G1/G0 and S/G2/M cells in the surface (5% of tumor diameter from bilateral edges) or central (total 10% from the center) region, are shown. Cell ratio indicates the ratio of S/G2/M phase cells to total cells. Red arrow indicates the region of the maximum fluorescence intensity emitted from G1/G0 cells (Rmax). Scale bar, 0.5 mm

(F) Representative microendoscopic images in the surface, center, and Rmax regions. Red and green fluorescence indicates G1/G0 and S/G2/M cells, respectively. Scale bar, 0.1 mm. Arrow (F.D.) indicates the traveling direction of the optical fiber.

(G) Endoscopic analysis of alterations in nuclear size of G1/G0 or S/G2/M cells. Red and green plots indicate G1/G0 and S/G2/M cells, respectively. The x axis indicates relative location in the longitudinal tumor (top = 0, bottom = 1).

(H) Representative microendoscopic image, with a frame extracted from arrow positions in (G), is shown. Arrowheads indicate abnormally large nuclei. Scale bar, 0.1 mm. Arrow (F.D.) indicates the traveling direction of the optical fiber.

(I) Endoscopic analysis of S/G2/M cell ratio in the surface and central regions. Data are presented as the mean ± SEM, n = 4 mice. *$p < 0.01$, based on Student's t test. (I′) Endoscopic analysis of nuclear size of cells in the surface and central regions. Data are presented as the mean ± SEM, n = 4 mice.

See also Videos S1 and S2.

Please cite this article in press as: Goto et al., Microendoscopy for periodic intravital end-to-end tumor imaging of cancer cells, Cell Reports Methods (2025), https://doi.org/10.1016/j.crmeth.2025.101056

CellPress
OPEN ACCESS

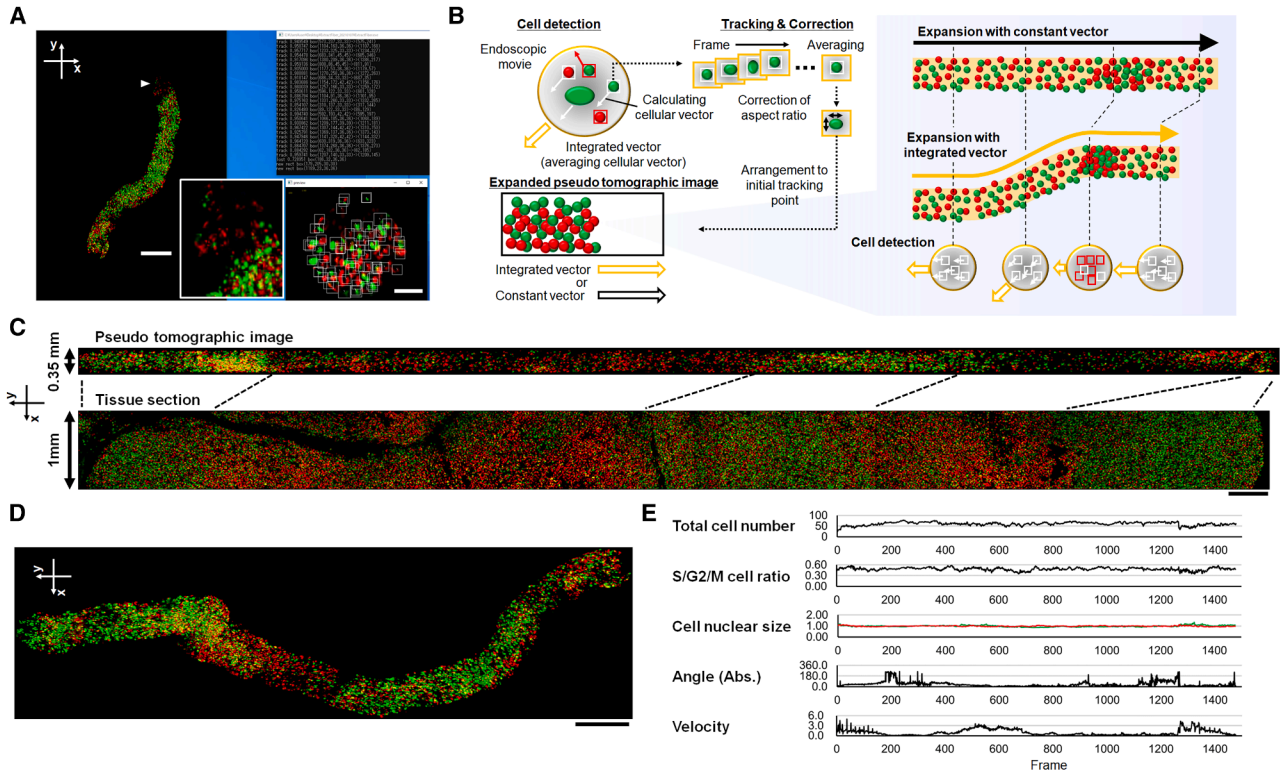

Figure 3. Pseudo-tomographic image synthesized from optical-fiber imaging video

(A) All data were obtained from one microendoscopic video of HT1080/Fucci(SA)5 cells in the xenograft tumor of cancer-bearing mice. Captured image showing the proceedings of the pseudo-tomographic image synthesis. The pseudo-tomographic image synthesis was running (left), and G1/G0 (red) and S/G2/M (green) cells were tracked into the bounding boxes in imaging window (right). Image in the small white rectangle shows enlarged image in the region indicated by arrowhead. Imaging window shows the image at the same region in the video. The horizontal and vertical axes are shown. Vertical axis corresponds to processing direction. Scale bars, 0.5 mm (pseudo-tomographic image) and 0.1 mm (imaging window).

(B) Schematic of the procedure of pseudo-tomographic image synthesis. Rectangles and arrows in the schematic of the endoscopic view indicate detected cells and cellular vectors, respectively. Extracted cells with (white) or without (red) the desired size and vector are indicated by color.

(C) Synthesized pseudo-tomographic image. The pseudo-tomographic image expanded with a constant vector (upper) and a confocal microscopic image of the fixed tissue section near the optical-fiber track (lower) are shown. The dotted lines show the border line of the area in which the cellular population correlates between the pseudo-tomographic and confocal images. The horizontal and vertical axes are shown. Vertical axis corresponds to processing direction. Scale bar, 0.5 mm

(D) Pseudo-tomographic image expanded with an integrated vector. The horizontal and vertical axes are shown. Vertical axis corresponds to processing direction. Scale bar, 0.5 mm

(E) Parameters obtained with pseudo-tomographic image synthesis. These parameters were calculated per frame and are shown with frame axis. The total cell number and S/G2/M cell ratio are shown. The red or green plots of nuclear size indicate G1/G0 and S/G2/M cells, respectively. The angle indicates arctan of tracked cells. Relative values with an average of all frames were calculated, and the absolute value is shown. The velocity indicates the number of tracked cells that migrate among frames. The relative values with an average of all frames were calculated.

(Figure 2 I′). Remarkably, G1/G0 cells with abnormal nuclear sizes were observed at the surface and center (Figure 2G, arrowheads in 2H). Thus, endoscopy enabled the repetitive spatiotemporal evaluation of the tumor tissue at the cellular level.

Generation of a pseudo-tomographic image from a microendoscopic video

We then tried to reconstruct the 2D pseudo-tomographic image from an endoscopic imaging video. This facilitated the recognition of cell-distribution patterns in entire tumors using the panoramic view. However, generating a 2D image using common panoramic image-generation procedures such as image mosaicing is difficult because the fluorescence intensity, relative position, and shape of objects among frames are slightly changed during the travel of the endomicroscopic probe. To generate the pseudo-tomographic image, we thus developed a program involving four steps (Figure 3A): (1) objects comparable in shape to the cell were extracted using the Laplacian of Gaussian filter (Figure 3B; cell detection), (2) extracted cells with the desired size and vector were tracked to distinguish them from cells adhered to the fiber and debris (Figure 3B; tracking and correction), (3) collected cell images during tracking were averaged (Figure 3B; tracking and correction), and (4) averaged cell images were arranged to coordinates based on the initial tracking point following aspect-ratio correction (Figure 3B; expanded pseudo-tomographic image). Coordinates of the initial tracking point were determined by the

Please cite this article in press as: Goto et al., Microendoscopy for periodic intravital end-to-end tumor imaging of cancer cells, Cell Reports Methods (2025), https://doi.org/10.1016/j.crmeth.2025.101056

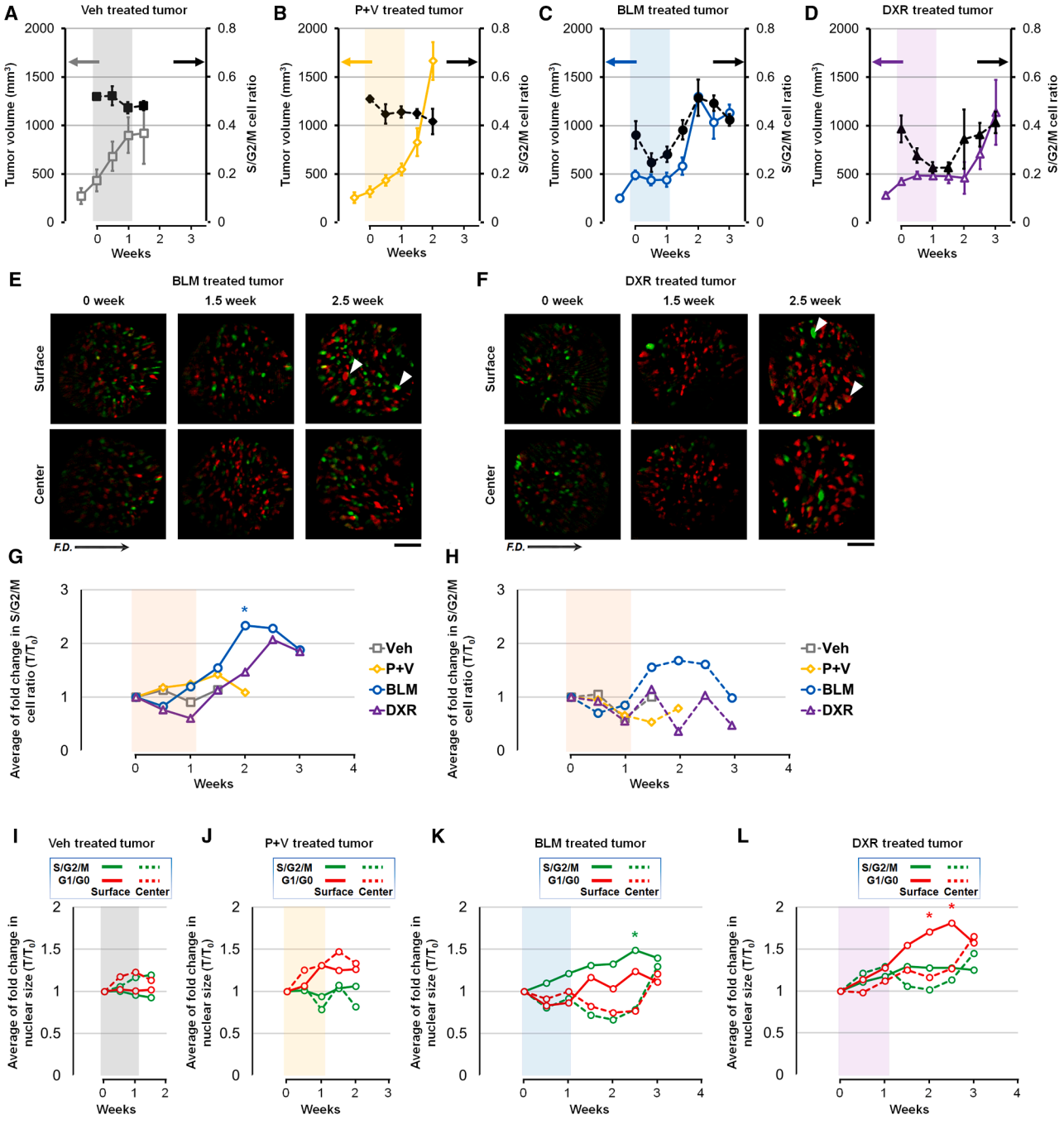

Figure 4. Fiber-bundle-based microendoscopic imaging system enables detailed assessment of anticancer drug efficacy

(A–D) BALB/c (nu/nu) nude mice were subcutaneously injected with 1.5×10^6 HT1080/Fucci(SA)5 cells. Tumor volume was measured twice per week. When the tumor size reached approximately 200–300 mm^3, microendoscopic imaging was initiated (week 0). Mice were administered (A) saline, (B) pazopanib (25 mg/kg) mixed with valproate (50 mg/kg) (PAZ + VAL), (C) bleomycin (20 mg/kg BLM), and (D) doxorubicin (3.8 mg/kg DXR) every 2 days for 8 days since week 0. Colored and black plots in each graph indicate the alterations in tumor volume and S/G2/M cell ratio analyzed using microendoscopy, respectively. Colored and black arrows indicate the *y* axis of colored and black plots, respectively. Color bars show the anticancer drug treatment period.

(E and F) Representative microendoscope images in the surface (upper) and central (lower) regions of a tumor treated with (E) BLM or (F) DXR in various time points in (C) and (D) (0 weeks, at the first imaging day of the first week; 1.5 weeks, at the second imaging day of the second week; 2.5 weeks, at the second imaging day of the third week). Red and green fluorescence indicates G1/G0 and S/G2/M cells, respectively. Arrowheads indicate the representative nuclear enlargement in the surface region. Scale bars, 0.1 mm. Arrow (F.D.) indicates the traveling direction of the optical fiber.

(legend continued on next page)

Please cite this article in press as: Goto et al., Microendoscopy for periodic intravital end-to-end tumor imaging of cancer cells, Cell Reports Methods (2025), https://doi.org/10.1016/j.crmeth.2025.101056

constant vector comprising a constant velocity (e.g., settings of the actuator) and an angle. The tomographic image showed similarities in the cell-distribution pattern with that of the confocal image; however, the relative positions of cell populations within each image were slightly different (Figure 3C). We attempted to generate the pseudo-tomographic image obtained by microendoscopy and confocal image from the close region in the same tumor. Nonetheless, it is technically challenging to obtain cryosectioned samples from the exact same tissue region in which microendoscopic imaging was performed. Subsequently, we developed an image based on the actual fiber tract that was corrected further because the direction and velocity of the fiber movement were slightly unstable owing to heterogeneous tissue stiffness. Thus, cells in the pseudo-tomographic image were arranged to the coordinates based on the integrated vector calculated from each tracking cell (Figure 3D). This allowed us to visualize the actual fiber tract. Moreover, our program could output parameters such as cell number and nuclear size, as well as direction and velocity, correlated with tissue stiffness (Figure 3E). Thus, our system can be utilized to analyze cell behavior more easily and tomographically by generating pseudo-tomographic images, further allowing us to analyze a mechanical parameter such as tissue stiffness.

Fiber-bundle-based microendoscopy enables detailed assessment of anticancer drug efficacy

We used a combination of HT1080/Fucci(SA)5 and our microendoscopy to evaluate the efficacy of the classical anticancer drugs, bleomycin and doxorubicin, which kill cancer cells by arresting cell-cycle progression followed by inflicting DNA double-strand breaks.[29,30] We also used the multikinase inhibitor pazopanib and histone deacetylase inhibitor valproate as representative molecular-targeting drugs. These two drugs were used together to inhibit tumor angiogenesis and induce sarcoma cell death without cell-cycle arrest.[31] Each drug was administered to the HT1080/Fucci(SA)5 mouse model every 2 days for 8 days from the point of first optical-fiber imaging when the tumor size reached approximately 200–300 mm^3 (Figures 4A–4D). Administration of bleomycin or doxorubicin resulted in tumor growth arrest, whereas pazopanib and valproate treatment only slightly inhibited tumor growth (Figures 4B–4D). One week after the final administration of bleomycin, the tumors started to grow again (Figure 4C). Of note, the regrowth of doxorubicin-treated tumors was slower than that of bleomycin-treated tumors (Figure 4D). Microendoscopic analysis showed that the S/G2/M cell ratios were closely correlated with these changes in tumor growth (Figures 4C–4F). In particular, the S/G2/M cell ratio was decreased after doxorubicin or bleomycin administration. Notably, the S/G2/M cell ratio in doxorubicin-treated tumors was slightly lower than that in bleomycin-treated tumors (Figures 4C–4F). In contrast, although treatment with pazopanib and valproate slightly reduced tumor growth, the S/G2/M cell ratio was not significantly different than that in the control group (Figures 4A and 4B). Because the endoscopic analysis of a tumor involves the evaluation of an individual tumor over a time course, the fold changes of each parameter can be calculated. During the administration of each drug, the fold changes in the S/G2/M cell ratio were decreased in the surface and central regions (Figures 4G, 4H, S3C, and S3D). After both doxorubicin and bleomycin administration, the increase in the S/G2/M cell ratio preceded tumor regrowth (Figures 4C and 4D). This increase in the S/G2/M cell ratio was observed at the surface and central regions. Remarkably, the S/G2/M cell ratio in bleomycin-treated tumors was higher than that in doxorubicin-treated tumors (Figures 4G, 4H S3C, and S3D). Additionally, these changes in the S/G2/M cell ratio in the doxorubicin-treated tumor were also observed in the tomographic image (Figure S3E). These results suggested that the efficacy of anticancer drugs, evaluated as tumor growth arrest, was positively correlated with changes in the cell-cycle state, which could be evaluated using microendoscopy *in vivo*. Microendoscopic images before, during, and after the administration of bleomycin or doxorubicin revealed an increase in the proportion of enlarged cell nuclei after drug administration (Figures 4E and 4F). The fold changes in the nuclear size in the bleomycin- or doxorubicin-administered tumors at a week after the final administration were significantly increased compared with those before administration; however, those in the control or pazopanib- and valproate-treated groups were not significantly changed (Figures 4I–4L and S3A–S3D). The analysis of fold changes showed that the nuclear enlargement of S/G2/M and G1/G0 cells was predominantly observed in bleomycin- and doxorubicin-treated tumors, respectively (Figures 4K, 4L, S3C, and S3D). Furthermore, the spatiotemporal analysis showed that the nuclear enlargement at the surface preceded that at the central region (Figures 4K, 4IL, S3C, and S3D). Two weeks after the final administration, enlarged nuclei emerged uniformly in both surface and central regions (Figures 4K, 4L, S3C, and S3D).

Finally, we attempted to provide insights into the correlations between the tumor growth speed, a kind of indicator for tumor malignancy, and the parameters including S/G2/M cell ratios or nuclear sizes in cancer cells obtained by the microendoscopic imaging following the withdrawal of anticancer drugs. Increased tumor regrowth speed showed a good correlation with the S/G2/M cell ratio in the surface region of the tumor after the final administration of doxorubicin or bleomycin (Figures S3F, S3G, S3J, and S3K). The nuclear enlargement in the surface region

(G and H) Endoscopic analysis of periodic alterations in the S/G2/M cell ratio of tumors treated with anticancer drugs. The average values of relative changes against those at the start of anticancer drug administration (T, value at each time point; T_0, value at the start of drug administration) in an individual tumor are shown. The graphs in (G) and (H) indicate values at the surface and central regions, respectively. Color bars show the anticancer drug treatment period.
(I–L) Endoscopic analysis of nuclear size in the surface (solid line) and central (dotted line) regions. The average values of relative changes against those at the start of anticancer drug administration (T, value at each time point; T_0, value at the start of drug administration) in an individual tumor treated with (I) Veh, (J) P + V, (K) BLM, and (L) DXR are shown. Color bars show the anticancer drug treatment period. Data are presented as the mean ± SEM, n = 6 mice (Veh), 6 mice (BLM), 7 mice (DXR), or four mice (PAZ + VAL). Notably, the numbers of used animals were reduced at certain time points (see Figures S3A–S3D) owing to death or lack of tumor solidity attributed to cachexia or anticancer drug treatment, thus interrupting endoscopic imaging. *$p < 0.05$, based on one-way ANOVA followed by the Tukey-Kramer test.

Please cite this article in press as: Goto et al., Microendoscopy for periodic intravital end-to-end tumor imaging of cancer cells, Cell Reports Methods (2025), https://doi.org/10.1016/j.crmeth.2025.101056

also showed the positive correlation only in G1/G0 cells in doxorubicin treatment, while this was shown in both G1/G0 cells and S/G2/M cells in bleomycin treatment (Figures S3F, S3H–S3J, S3l, and S3M). Those findings suggested that S/G2/M cell ratio and nuclear enlargement at the surface region of tumor could be indicators for malignancy in chemotherapy. These results indicate that microendoscopic imaging allows us to obtain extensive knowledge in medical and pharmaceutical research as well as biological research.

DISCUSSION

Existing imaging devices have limitations in terms of resolution, invasiveness, and imaging depth, hindering the observation of spatiotemporal cellular dynamics in tumors. Although multiphoton microscopy has been used to examine the tumor environment and efficacy of anticancer drugs *in vivo*, its depth range is limited to approximately 1.0 mm from the tumor surface, and visualization of deeper areas remains challenging. Therefore, we developed a new imaging technique that allows for a greater visualization depth. We combined a fiber-bundle-based microendoscope with a sharpened tip and genetically encoded Fucci. The introduction of a bamboo spear-shaped imaging probe allowed for the analysis of microscopic objects without complicated optical corrections (Figure 1A). Moreover, the microendoscope was equipped with a multicolor laser system and provided cellular resolution, enabling the clear observation of beads with a diameter of 2 μm (Figure 1B). The spatial resolution in our system is limited by core diameter of single-mode optical fiber composed of optical-fiber bundle. The use of optical fiber with a core diameter of 2 μm is thought to archive visualization of the 2-μm beads in this study. The substantial field of view is defined by the diameter of the optical-fiber bundle. Although we applied a 350-μm diameter of the optical-fiber bundle in the present study, it can be more than twice the size of the field of view for commercial purposes. However, there is a trade-off between field of view and invasiveness. The frame rate and image resolution depend on the number of scanning vertical lines; in this study, the frame rate was 7.5 fps owing to the acquisition of line numbers for image resolution. Thus, the frame rate can also be increased by reducing the number of scanning vertical lines. The scan depth of our imaging probe was calculated at approximately 13.8 μm (Figure 2A). This limitation of scan depth is considered to be due to the optical properties of imaging tissue and diverging of exciting light. The acquisition of end-to-end imaging data took 2–3 min even in a tumor of 1 cm in diameter using an optical-fiber bundle running at 0.069 mm/s (Video S1), indicating that the imaging system achieved high-throughput performance with minimal invasiveness (Figures 1D and 1E). The cell-distribution pattern in longitudinal imaging using endoscopy is closely correlated with that in the histological image obtained from confocal microscopic imaging (Figures 2B and 2C). Cellular information such as the nuclear size and proliferating activity could be obtained not only over the desired time course but also at the desired imaging depth (Figures 2D–2I′). Such endoscopic performance can largely contribute to experimental animal ethics. High-throughput performance and low invasiveness are expected to reduce animal suffering. Moreover, periodic intravital imaging can significantly reduce the number of experimental animals used.

In its original form, microendoscopy provided an imaging video. Here, we succeeded in reconstructing a 2D pseudo-tomographic image from this imaging video (Figures 3, S3E, and S5C). This pseudo-tomographic image allowed us to comprehensively and easily recognize the cell-distribution pattern in the panoramic view. It showed similarities in the cell-distribution pattern with that of the confocal image in the same tumor (Figure 3C). However, the relative positions of cell populations were slightly different between the pseudo-tomographic image and the confocal image. In addition, microendoscopic analysis of the S/G2/M cell ratio in the surface region was slightly higher than the confocal image (Figure S2B). These inconsistencies might be due to the technical difficulty of obtaining cryo-sectioned samples from the same tissue region in which microendoscopic imaging was performed. The tract of fiber and insertion point were hardly recognized because of low invasiveness. Moreover, the process of specimen preparation, including resection, chemical fixation, and cryo-sectioning, causes various artificial effects such as tissue folding, shrinkage, and changes in autofluorescence. Thus, it is suggested that the difference in S/G2/M cell ratio between microendoscopy and confocal microscopy occurred in association with various artificial effects during specimen preparation. Thereby, it is thought that intravital monitoring of cellular and molecular dynamics is important for a clear understanding of pathophysiology. In addition, mechanical parameters could be concurrently obtained with the localization pattern of the cell population (Figure 3E). Recent studies reported that mechanical parameters surrounding cells affect cellular behavior, including cancer malignancy.[32,33] Other biological information regarding blood vessels, extracellular matrix, and cellular architecture can be also obtained using genetically encoded and fluorescent probes. The microendoscopic system will facilitate the visualization of this critical biological information, thereby aiding in the disclosure of the mechanism of cancer malignancy.

Using microendoscopy, we successfully visualized the efficacy of anticancer drugs at a cellular-level resolution in tumors (Figure 4). In this study, three types of anticancer drugs, pazopanib, bleomycin, and doxorubicin, were tested. Doxorubicin and bleomycin are cell-cycle-specific drugs that induce DNA double-strand damage.[29,30] Pazopanib is an angiogenesis inhibitor that starves cancer cells and ultimately inhibits their proliferation.[31] In our experiments, tumor growth was significantly inhibited by doxorubicin or bleomycin but not by pazopanib at the doses used (Figures 4A–4D). The proliferating cancer cell ratio (S/G2/M cell ratio) was consistently decreased following treatment with doxorubicin or bleomycin (Figures 4C and 4D) but not after treatment with pazopanib (Figure 4B). Furthermore, tumor regrowth speed correlated with the cell-proliferation ratio after chemotherapy (Figures 4C and 4D). Anticancer drug treatment led to an increase in the number of enlarged nuclei (Figures 4E, 4F, 4K, and 4L). Different anticancer drugs resulted in the emergence of different spatiotemporal patterns of enlarged nuclei and cell-cycle states. For instance, many enlarged nuclei were observed in proliferating cells in

Please cite this article in press as: Goto et al., Microendoscopy for periodic intravital end-to-end tumor imaging of cancer cells, Cell Reports Methods (2025), https://doi.org/10.1016/j.crmeth.2025.101056

bleomycin-treated tumors and in nonproliferating cells in doxorubicin-treated tumors (Figures 4K and 4L). Confocal laser microscopic images consistently showed enlargement of cancer cell nuclei as visualized by DNA staining with each Fucci signal in the doxorubicin-treated tumor (Figure S4). In some *in vitro* studies, emergence of nuclear enlargement of cancer cells under the doxorubicin and bleomycin treatments has been also reported.[34–36] In addition, evaluating severe cellular conditions, such as hypoxia (low oxygen supply or $CoCl_2$ treatment)[37,38] or anticancer drug treatment,[39–41] have demonstrated similar nuclear enlargement through cell-cycle arrest, cell fusion, or endoreplication. Pathological studies have also shown that enlarged nuclei are frequently observed in high-grade or postchemotherapeutic tumors.[42,43] Thus, nuclear enlargement of cancer cells has been discussed to be involved in cancer malignancy; however, a limited number of studies have been reported in animal models *in vivo*. Our findings regarding nuclear enlargement are expected to contribute to the understanding of cellular response *in vivo* to anticancer drugs. Nuclear enlargement in our study was observed to occur preferentially on the surface of tumors treated with either bleomycin or doxorubicin. Microendoscopy also revealed that the tumor surface was predominantly occupied by proliferating cells (Figure 2I), suggesting that many enlarged nuclei were induced by mitotic interference following impaired DNA replication. Vascular density was higher at the surface region of the tumor than at the central region (Figures S2C–S2E). The distribution of doxorubicin within the tumor has shown a gradual pattern according to the distance to blood vessels.[44,45] Thus, previous studies support our findings that polyploid cancer cells arise with spatiotemporal heterogeneity in tumors after doxorubicin or bleomycin administration. Furthermore, tumor regrowth speed after anticancer drug treatment showed a correlation with nuclear enlargement in cancer cells (Figures S3F–S3M). This suggests that cancer cells with enlarged nuclei have the potential of reproliferation after anticancer treatments resulting in drug resistance and cancer recurrence. Meanwhile, we showed that the S/G2/M cell ratio changed with the increase in tumor volume (Figures 2D and 2D′). These data indicate that a heterogeneous tumor environment is formed along with the tumor growth and/or the time after tumor cell transplant. Therefore, the administration of anticancer drugs at an appropriate time can be evaluated for effect on the more heterogeneous tumor environment. Simultaneously, we should carefully examine the experimental endpoint (i.e., tumor expansion and loss of body weight related to the cachexia and anticancer drug). Thus, the assessment of anticancer drug effects in a more heterogeneous tumor environment will be addressed in the next study.

Although we have shown important oncological and cell biological findings in this study, our technique can be expected in clinical applications such as the evaluation of cancer therapies (e.g., chemotherapy, radiotherapy, and immunotherapy), diagnosis of cancer cell genotype and phenotype, and intraoperative diagnosis. With the development of next-generation sequencers, genetic diagnosis is more advanced and enables advanced cancer therapies such as precision medicine. Genotype and phenotype of cancer cells alter spatiotemporally in the tumor.[46–49] In addition, some cancer therapies are well known to trigger the genomic mutation in cancer cells.[50,51] This genotypic and phenotypic heterogeneity is a crucial factor in cancer recurrence and drug resistance. There is a possibility that our technique can spatiotemporally assess the phenotype of cancer cells even before and after cancer therapies. In addition, degrees of infiltration and accumulation of immune cells into tumors are effective indicators for immunotherapeutic effect,[52,53] which our technique may also assess because it allows for visualization spatiotemporally at cellular resolution. Therefore, our technique has potential for medical applications and can make advanced cancer therapies more effective. Moreover, our technique combined with other clinical modalities such as sonography and conventional endoscopy can be a strong clinical tool because of realizable macro- and microscopic diagnosis. Currently, clinical and intravital imaging devices have advanced in many technological aspects, including field of view, spatial resolution, and functional imaging.[9,11,13,54,55] However, these remain difficult to visualize at the single-cell resolution. Our technique combined with existing clinical devices is expected to innovate novel clinical technologies such as novel intraoperative diagnosis methods.

Clinical application of our technique is challenging and there are some subjects including fluorescence labeling and imaging in the internal organ. Owing to progress of biochemistry and synthetic chemistry, various fluorescence dyes have been developed for the fluorescence labeling of cells. Currently, some of them are being studied in clinical trials.[56] Moreover, several antibody drugs have been developed, and some radioisotope or photosensitizer-labeled antibody drugs have been approved by the United States Food and Drug Administration.[57,58] Thus, there is a possibility that fluorescence-labeled antibody drugs will spread as diagnostic drugs, which would support the clinical application of our technique. In addition, demonstrating that microendoscopic imaging can be performed within the internal organs is essential for clinical applications. Our technique will require an evaluation in the orthotopic transplant and spontaneous carcinogenesis models. Our preliminary study showed that the microendoscopic system successfully visualized the glioma cells in the glioma mouse model as the orthotopic transplant model (Figure S5 and Video S3). These preliminary data suggest that our technique can be applied to the *in vivo* cellular imaging in the orthotopic transplant model in deeper internal organs than subcutaneous tissue.

In conclusion, this imaging system contributes greatly to the development of tumor biology and anticancer therapies by enabling a better understanding of the precise mechanism by which tumors respond to or resist anticancer therapies.

Limitations of the study

Our microendoscopic system successfully achieved the spatiotemporal analysis of the proliferative behavior of cancer cells through less invasive, repetitive, and end-to-end tumor imaging *in vivo*. The time required to obtain the images in each tumor was only 2–3 min, highlighting the super-high-throughput imaging capabilities of the microendoscopic system. The system enabled the visualization of the efficacy of anticancer drugs in heterogeneous cancer micro- and macroenvironments, indicating its

usefulness in optimizing anticancer strategies and assessing drug efficacy. However, our system was limited in its observation of 2-μm beads because of the diameter of each optical-fiber core. Therefore, applying our system for imaging that requires a high resolution, such as imaging of chromatin patterns and organelle dynamics, is difficult. In this study, Fucci(SA)5 was applied to microendoscopic imaging and succeeded in clear imaging of cell-cycle state in G1/G0 and S/G2/M phase *in vivo*. Furthermore, Fucci(CA)5 can clearly visualize the S and G2 phases separately.[26] A future challenge is to obtain precise cell-cycle information *in vivo* through imaging of Fucci(CA)5 and combination with other indicators. Moreover, distance to blood vessels and hypoxia are crucial factors for understanding of tumor environment and response to anticancer drugs. Our technique will visualize the hypoxic area by using hypoxia-sensitive fluorescence probes in the future.

RESOURCE AVAILABILITY

Lead contact

Requests for further information and resources should be directed to and will be fulfilled by the lead contact, Yosky Kataoka (kataokay@person.kobe-u.ac.jp).

Materials availability

HT1080/Fucci(SA)5 (clone #2) (RCB 4698) cells were provided by the RIKEN BioResource Research Center (BRC) Cell Bank (https://cell.brc.riken.jp/en/). Information about Fucci-related materials is available on the website (https://cfds.riken.jp/material/fucci).

Data and code availability

- All data reported in this paper will be shared by lead contact upon request.
- All original code has been deposited at Open Science Framework (OSF): https://osf.io/8345y/files/osfstorage?view_only=4d6af5e5bc054582a7ad369147e62e19. An archival DOI is listed in the key resources table.
- Any additional information required to re-analyze the data reported in this paper is available from the lead contact upon request.

ACKNOWLEDGMENTS

This work was supported in part by grants from the Japan Ministry of Education, Culture, Sports, Science and Technology Grant-in-Aid for Scientific Research (B) (18H02724 and 21H02787 to Y.K., 19H03140 to A.S.-S.), Grant-in-Aid for Scientific Research (S) (21H05041 to A. Miyawaki), Grant-in-Aid for Specially Promoted Research (19H05462 to Y.K.), Scientific Research on Innovative Areas: Resonance Bio (15H05948 to A. Miyawaki), and the Brain Mapping by Integrated Neurotechnologies for Disease Studies (Brain/MINDS) from Japan Agency for Medical Research and Development (AMED) (JP15dm0207001 to A. Miyawaki), the Japan Science and Technology Agency (JST) CREST (JPMJCR2124 to A.S.-S.), Research Foundation for Opto-Science and Technology (to Y.K.), and the Uehara Memorial Foundation (to K.F.). This study was partially supported by AMED Practical Research Project for Rare/Intractable Diseases 2021–2023 (23ek0109517h0001 to A. Mizoguchi). We gratefully acknowledge Dr. Ryoko Ando and Ms. Keiko Shoda for their support in establishing the HT1080/Fucci(SA)5 cell line.

AUTHOR CONTRIBUTIONS

T.G., M.N., and S.D. generated the cancer-bearing mice, performed *in vivo* microendoscopy experiments and data analysis, and drafted the manuscript. C. U. and A.W. prepared HT1080 cells expressing tFucci(SA)5 and performed histochemical experiments using confocal laser microscopy. A.S.-S. and A. Miyawaki established the HT1080/Fucci(SA)5 cell line, advised on the system, and assisted with manuscript preparation. I.N. developed a computer program for obtaining pseudo-tomographic images from microendoscopic videos. T.N. and Y.T. advised on histological analysis and assisted with manuscript preparation. A. Mizoguchi advised on microendoscopy optics and the application design and assisted with manuscript preparation. K.M. performed statistical data analysis. Y.K. supervised the experimental design, data analysis, cancer cell biology interpretations, and manuscript preparation. K.F. supervised the experimental design, application of microendoscopy, and manuscript preparation. All authors contributed to the writing of the manuscript before submission.

DECLARATION OF INTERESTS

T.G., S.D., I.N., A. Mizoguchi, K.F., and Y.K. are inventors on patent no. PCT/JP2022/015824, which covers the pseudo-tomographic image synthesis program. A.S.-S. and A. Miyawaki are inventors on Japanese patent no. 5370890, US patent no. 8182987, and EP patent no. 2138577, which covers the creation and use of Fucci.

STAR★METHODS

Detailed methods are provided in the online version of this paper and include the following:

- KEY RESOURCES TABLE
- EXPERIMENTAL MODEL AND STUDY PARTICIPANT DETAILS
  - Cell lines
  - Tumor xenograft models
- METHOD DETAILS
  - Cell culture
  - Animal study
  - *In vivo* microendoscopic imaging
  - Image processing
  - Pseudo-tomographic image synthesis
  - Histological analysis
- QUANTIFICATION AND STATISTICAL ANALYSIS

SUPPLEMENTAL INFORMATION

Supplemental information can be found online at https://doi.org/10.1016/j.crmeth.2025.101056.

Received: September 4, 2024
Revised: February 20, 2025
Accepted: May 12, 2025
Published: June 4, 2025

REFERENCES

1. Wang, R.A., Li, Q.L., Li, Z.S., Zheng, P.J., Zhang, H.Z., Huang, X.F., Chi, S. M., Yang, A.G., and Cui, R. (2013). Apoptosis drives cancer cells proliferate and metastasize. J. Cell Mol. Med. *17*, 205–211. https://doi.org/10.1111/j.1582-4934.2012.01663.x.
2. Quail, D.F., and Joyce, J.A. (2013). Microenvironmental regulation of tumor progression and metastasis. Nat. Med. *19*, 1423–1437. https://doi.org/10.1038/nm.3394.
3. Joyce, J.A., and Pollard, J.W. (2009). Microenvironmental regulation of metastasis. Nat. Rev. Cancer *9*, 239–252. https://doi.org/10.1038/nrc2618.
4. Albini, A., and Sporn, M.B. (2007). The tumour microenvironment as a target for chemoprevention. Nat. Rev. Cancer *7*, 139–147. https://doi.org/10.1038/nrc2067.
5. Brown, J.M. (1999). The hypoxic cell: a target for selective cancer therapy–eighteenth Bruce F. Cain Memorial Award lecture. Cancer Res. *59*, 5863–5870.

6. Ortmann, B., Druker, J., and Rocha, S. (2014). Cell cycle progression in response to oxygen levels. Cell. Mol. Life Sci. *71*, 3569–3582. https://doi.org/10.1007/s00018-014-1645-9.

7. Kizaka-Kondoh, S., Inoue, M., Harada, H., and Hiraoka, M. (2003). Tumor hypoxia: a target for selective cancer therapy. Cancer Sci. *94*, 1021–1028. https://doi.org/10.1111/j.1349-7006.2003.tb01395.x.

8. Höckel, M., and Vaupel, P. (2001). Tumor hypoxia: definitions and current clinical, biologic, and molecular aspects. J. Natl. Cancer Inst. *93*, 266–276. https://doi.org/10.1093/jnci/93.4.266.

9. Clark, D.P., and Badea, C.T. (2021). Advances in micro-CT imaging of small animals. Phys. Med. *88*, 175–192. https://doi.org/10.1016/j.ejmp.2021.07.005.

10. Schmidt, E.L., Ou, Z., Ximendes, E., Cui, H., Keck, C.H.C., Jaque, D., and Hong, G. (2024). Near-infrared II fluorescence imaging. Nat. Rev. Methods Primers *4*, 23. https://doi.org/10.1038/s43586-024-00301-x.

11. Song, P., Rubin, J.M., and Lowerison, M.R. (2023). Super-resolution ultrasound microvascular imaging: is it ready for clinical use? Z. Med. Phys. *33*, 309–323. https://doi.org/10.1016/j.zemedi.2023.04.001.

12. Christensen-Jeffries, K., Couture, O., Dayton, P.A., Eldar, Y.C., Hynynen, K., Kiessling, F., O'Reilly, M., Pinton, G.F., Schmitz, G., Tang, M.X., et al. (2020). Super-resolution ultrasound imaging. Ultrasound Med. Biol *46*, 865–891. https://doi.org/10.1016/j.ultrasmedbio.2019.11.013.

13. Feinberg, D.A., Beckett, A.J.S., Vu, A.T., Stockmann, J., Huber, L., Ma, S., Ahn, S., Setsompop, K., Cao, X., Park, S., et al. (2023). Next-generation MRI scanner designed for ultra-high-resolution human brain imaging at 7 Tesla. Nat. Methods *20*, 2048–2057. https://doi.org/10.1038/s41592-023-02068-7.

14. Boulant, N., Mauconduit, F., Gras, V., Amadon, A., Le Ster, C., Luong, M., Massire, A., Pallier, C., Sabatier, L., Bottlaender, M., et al. (2024). In vivo imaging of the human brain with the Iseult 11.7-T MRI scanner. Nat. Methods *21*, 2013–2016. https://doi.org/10.1038/s41592-024-02472-7.

15. Sugita, S., Yamato, M., Hatabu, T., and Kataoka, Y. (2021). Involvement of cancer-derived EMT cells in the accumulation of 18F-fluorodeoxyglucose in the hypoxic cancer microenvironment. Sci. Rep. *11*, 9668. https://doi.org/10.1038/s41598-021-88414-1.

16. Kagawa, Y., Matsumoto, S., Kamioka, Y., Mimori, K., Naito, Y., Ishii, T., Okuzaki, D., Nishida, N., Maeda, S., Naito, A., et al. (2013). Cell cycle-dependent Rho GTPase activity dynamically regulates cancer cell motility and invasion in vivo. PLoS One *8*, e83629. https://doi.org/10.1371/journal.pone.0083629.

17. Ricard, C., Tchoghandjian, A., Luche, H., Grenot, P., Figarella-Branger, D., Rougon, G., Malissen, M., and Debarbieux, F. (2016). Phenotypic dynamics of microglial and monocyte-derived cells in glioblastoma-bearing mice. Sci. Rep. *6*, 26381. https://doi.org/10.1038/srep26381.

18. Xu, C., Nedergaard, M., Fowell, D.J., Friedl, P., and Ji, N. (2024). Multiphoton fluorescence microscopy for in vivo imaging. Cell *187*, 4458–4487. https://doi.org/10.1016/j.cell.2024.07.036.

19. Escobet-Montalbán, A., Gasparoli, F.M., Nylk, J., Liu, P., Yang, Z., and Dholakia, K. (2018). Three-photon light-sheet fluorescence microscopy. Opt. Lett. *43*, 5484–5487. https://doi.org/10.1364/OL.43.005484.

20. Wang, F., Wan, H., Ma, Z., Zhong, Y., Sun, Q., Tian, Y., Qu, L., Du, H., Zhang, M., Li, L., et al. (2019). Light-sheet microscopy in the near-infrared II window. Nat. Methods *16*, 545–552. https://doi.org/10.1038/s41592-019-0398-7.

21. Goto, A., Nakahara, I., Yamaguchi, T., Kamioka, Y., Sumiyama, K., Matsuda, M., Nakanishi, S., and Funabiki, K. (2015). Circuit-dependent striatal PKA and ERK signaling underlies rapid behavioral shift in mating reaction of male mice. Proc. Natl. Acad. Sci. USA *112*, 6718–6723. https://doi.org/10.1073/pnas.1507121112.

22. Yamaguchi, T., Goto, A., Nakahara, I., Yawata, S., Hikida, T., Matsuda, M., Funabiki, K., and Nakanishi, S. (2015). Role of PKA signaling in D2 receptor-expressing neurons in the core of the nucleus accumbens in aversive learning. Proc. Natl. Acad. Sci. USA *112*, 11383–11388. https://doi.org/10.1073/pnas.1514731112.

23. Isosaka, T., Matsuo, T., Yamaguchi, T., Funabiki, K., Nakanishi, S., Kobayakawa, R., and Kobayakawa, K. (2015). Htr2a-expressing cells in the central amygdala control the hierarchy between innate and learned fear. Cell *163*, 1153–1164. https://doi.org/10.1016/j.cell.2015.10.047.

24. Monfared, A., Blevins, N.H., Cheung, E.L.M., Jung, J.C., Popelka, G., and Schnitzer, M.J. (2006). In vivo imaging of mammalian cochlear blood flow using fluorescence microendoscopy. Otol. Neurotol. *27*, 144–152. https://doi.org/10.1097/01.mao.0000190708.44067.b0.

25. Sakaue-Sawano, A., Kurokawa, H., Morimura, T., Hanyu, A., Hama, H., Osawa, H., Kashiwagi, S., Fukami, K., Miyata, T., Miyoshi, H., et al. (2008). Visualizing spatiotemporal dynamics of multicellular cell-cycle progression. Cell *132*, 487–498. https://doi.org/10.1016/j.cell.2007.12.033.

26. Ando, R., Sakaue-Sawano, A., Shoda, K., and Miyawaki, A. (2023). Two coral fluorescent proteins of distinct colors for sharp visualization of cell-cycle progression. Cell Struct. Funct. *48*, 135–144. https://doi.org/10.1247/csf.23028.

27. Yashiro, H., Nakahara, I., Funabiki, K., and Riquimaroux, H. (2017). Microendoscopic system for functional assessment of neural circuits in deep brain regions: simultaneous optical and electrical recordings of auditory responses in mouse's inferior colliculus. Neurosci. Res. *119*, 61–69. https://doi.org/10.1016/j.neures.2017.01.002.

28. Sakaue-Sawano, A., Yo, M., Komatsu, N., Hiratsuka, T., Kogure, T., Hoshida, T., Goshima, N., Matsuda, M., Miyoshi, H., and Miyawaki, A. (2017). Genetically encoded tools for optical dissection of the mammalian cell cycle. Mol. Cell *68*, 626–640.e5. https://doi.org/10.1016/j.molcel.2017.10.001.

29. Chen, J., and Stubbe, J. (2005). Bleomycins: towards better therapeutics. Nat. Rev. Cancer *5*, 102–112. https://doi.org/10.1038/nrc1547.

30. Thorn, C.F., Oshiro, C., Marsh, S., Hernandez-Boussard, T., McLeod, H., Klein, T.E., and Altman, R.B. (2011). Doxorubicin pathways: pharmacodynamics and adverse effects. Pharmacogenet. Genomics *21*, 440–446. https://doi.org/10.1097/FPC.0b013e32833ffb56.

31. Tavallai, S., Hamed, H.A., Grant, S., Poklepovic, A., and Dent, P. (2014). Pazopanib and HDAC inhibitors interact to kill sarcoma cells. Cancer Biol. Ther *15*, 578–585. https://doi.org/10.4161/cbt.28163.

32. Cambria, E., Coughlin, M.F., Floryan, M.A., Offeddu, G.S., Shelton, S.E., and Kamm, R.D. (2024). Linking cell mechanical memory and cancer metastasis. Nat. Rev. Cancer *24*, 216–228. https://doi.org/10.1038/s41568-023-00656-5.

33. Mao, Y., and Wickström, S.A. (2024). Mechanical state transitions in the regulation of tissue form and function. Nat. Rev. Mol. Cell Biol. *25*, 654–670. https://doi.org/10.1038/s41580-024-00719-x.

34. Nakayama, Y., Igarashi, A., Kikuchi, I., Obata, Y., Fukumoto, Y., and Yamaguchi, N. (2009). Bleomycin-induced over-replication involves sustained inhibition of mitotic entry through the ATM/ATR pathway. Exp. Cell Res. *315*, 2515–2528. https://doi.org/10.1016/j.yexcr.2009.06.007.

35. Mosieniak, G., Sliwinska, M.A., Alster, O., Strzeszewska, A., Sunderland, P., Piechota, M., Was, H., and Sikora, E. (2015). Polyploidy Formation in Doxorubicin-Treated Cancer Cells Can Favor Escape from Senescence. Neoplasia *17*, 882–893. https://doi.org/10.1016/j.neo.2015.11.008.

36. Hayashi, K., Horisaka, K., Harada, Y., Ogawa, Y., Yamashita, T., Kitano, T., Wakita, M., Fukusumi, T., Inohara, H., Hara, E., and Matsumoto, T. (2024). Polyploidy mitigates the impact of DNA damage while simultaneously bearing its burden. Cell Death Discov. *10*, 436. https://doi.org/10.1038/s41420-024-02206-w.

37. Zhang, S., Mercado-Uribe, I., Xing, Z., Sun, B., Kuang, J., and Liu, J. (2014). Generation of cancer stem-like cells through the formation of polyploid giant cancer cells. Oncogene *33*, 116–128. https://doi.org/10.1038/onc.2013.96.

38. Yart, L., Bastida-Ruiz, D., Allard, M., Dietrich, P.Y., Petignat, P., and Cohen, M. (2022). Linking unfolded protein response to ovarian cancer cell

fusion. BMC Cancer *22*, 622. https://doi.org/10.1186/s12885-022-09648-4.

39. Niu, N., Mercado-Uribe, I., and Liu, J. (2017). Dedifferentiation into blastomere-like cancer stem cells via formation of polyploid giant cancer cells. Oncogene *36*, 4887–4900. https://doi.org/10.1038/onc.2017.72.
40. Sakaue-Sawano, A., Kobayashi, T., Ohtawa, K., and Miyawaki, A. (2011). Drug-induced cell cycle modulation leading to cell-cycle arrest, nuclear mis-segregation, or endoreplication. BMC Cell Biol. *12*, 2. https://doi.org/10.1186/1471-2121-12-2.
41. Niu, N., Zhang, J., Zhang, N., Mercado-Uribe, I., Tao, F., Han, Z., Pathak, S., Multani, A.S., Kuang, J., Yao, J., et al. (2016). Linking genomic reorganization to tumor initiation via the giant cell cycle. Oncogenesis *5*, e281. https://doi.org/10.1038/oncsis.2016.75.
42. Fei, F., Zhang, D., Yang, Z., Wang, S., Wang, X., Wu, Z., Wu, Q., and Zhang, S. (2015). The number of polyploid giant cancer cells and epithelial-mesenchymal transition-related proteins are associated with invasion and metastasis in human breast cancer. J. Exp. Clin. Cancer Res. *34*, 158. https://doi.org/10.1186/s13046-015-0277-8.
43. Qu, Y., Zhang, L., Rong, Z., He, T., and Zhang, S. (2013). Number of glioma polyploid giant cancer cells (PGCCs) associated with vasculogenic mimicry formation and tumor grade in human glioma. J. Exp. Clin. Cancer Res. *32*, 75. https://doi.org/10.1186/1756-9966-32-75.
44. Lankelma, J., Dekker, H., Luque, F.R., Luykx, S., Hoekman, K., van der Valk, P., van Diest, P.J., and Pinedo, H.M. (1999). Doxorubicin gradients in human breast cancer. Clin. Cancer Res. *5*, 1703–1707.
45. Primeau, A.J., Rendon, A., Hedley, D., Lilge, L., and Tannock, I.F. (2005). The distribution of the anticancer drug Doxorubicin in relation to blood vessels in solid tumors. Clin. Cancer Res. *11*, 8782–8788. https://doi.org/10.1158/1078-0432.CCR-05-1664.
46. Gao, D., Mittal, V., Ban, Y., Lourenco, A.R., Yomtoubian, S., and Lee, S. (2018). Metastatic tumor cells - genotypes and phenotypes. Front. Biol. *13*, 277–286. https://doi.org/10.1007/s11515-018-1513-3.
47. Sonugür, F.G., and Akbulut, H. (2019). The Role of Tumor Microenvironment in Genomic Instability of Malignant Tumors. Front. Genet. *10*, 1063. https://doi.org/10.3389/fgene.2019.01063.
48. Bhandari, V., Li, C.H., Bristow, R.G., and Boutros, P.C.; PCAWG Consortium (2020). Divergent mutational processes distinguish hypoxic and normoxic tumours. Nat. Commun. *11*, 737. https://doi.org/10.1038/s41467-019-14052-x.
49. Whiting, F.J.H., Househam, J., Baker, A.M., Sottoriva, A., and Graham, T. A. (2024). Phenotypic noise and plasticity in cancer evolution. Trends Cell Biol. *34*, 451–464. https://doi.org/10.1016/j.tcb.2023.10.002.
50. Behjati, S., Gundem, G., Wedge, D.C., Roberts, N.D., Tarpey, P.S., Cooke, S.L., Van Loo, P., Alexandrov, L.B., Ramakrishna, M., Davies, H., et al. (2016). Mutational signatures of ionizing radiation in second malignancies. Nat. Commun. *7*, 12605. https://doi.org/10.1038/ncomms12605.
51. Pich, O., Muiños, F., Lolkema, M.P., Steeghs, N., Gonzalez-Perez, A., and Lopez-Bigas, N. (2019). The mutational footprints of cancer therapies. Nat. Genet. *51*, 1732–1740. https://doi.org/10.1038/s41588-019-0525-5.
52. Darvin, P., Toor, S.M., Sasidharan Nair, V., and Elkord, E. (2018). Immune checkpoint inhibitors: recent progress and potential biomarkers. Exp. Mol. Med. *50*, 1–11. https://doi.org/10.1038/s12276-018-0191-1.
53. Skovgard, M.S., Hocine, H.R., Saini, J.K., Moroz, M., Bellis, R.Y., Banerjee, S., Morello, A., Ponomarev, V., Villena-Vargas, J., and Adusumilli, P.S. (2021). Imaging CAR T-cell kinetics in solid tumors: Translational implications. Mol. Ther. Oncolytics *22*, 355–367. https://doi.org/10.1016/j.omto.2021.06.006.
54. Bodea, S.V., and Westmeyer, G.G. (2021). Photoacoustic Neuroimaging - Perspectives on a Maturing Imaging Technique and its Applications in Neuroscience. Front. Neurosci. *15*, 655247. https://doi.org/10.3389/fnins.2021.655247.
55. Bouma, B.E., de Boer, J.F., Huang, D., Jang, I.K., Yonetsu, T., Leggett, C. L., Leitgeb, R., Sampson, D.D., Suter, M., Vakoc, B., et al. (2022). Optical coherence tomography. Nat. Rev. Methods Primers *2*, 79. https://doi.org/10.1038/s43586-022-00162-2.
56. Seah, D., Cheng, Z., and Vendrell, M. (2023). Fluorescent Probes for Imaging in Humans: Where Are We Now? ACS Nano *17*, 19478–19490. https://doi.org/10.1021/acsnano.3c03564.
57. Boswell, C.A., and Brechbiel, M.W. (2007). Development of radioimmunotherapeutic and diagnostic antibodies: an inside-out view. Nucl. Med. Biol. *34*, 757–778. https://doi.org/10.1016/j.nucmedbio.2007.04.001.
58. Mitsunaga, M., Ogawa, M., Kosaka, N., Rosenblum, L.T., Choyke, P.L., and Kobayashi, H. (2011). Cancer cell–selective in vivo near infrared photoimmunotherapy targeting specific membrane molecules. Nat. Med. *17*, 1685–1691. https://doi.org/10.1038/nm.2554.
59. Schindelin, J., Arganda-Carreras, I., Frise, E., Kaynig, V., Longair, M., Pietzsch, T., Preibisch, S., Rueden, C., Saalfeld, S., Schmid, B., et al. (2012). Fiji: an open-source platform for biological-image analysis. Nat. Methods *9*, 676–682. https://doi.org/10.1038/nmeth.2019.
60. Nussbaum-Krammer, C.I., Neto, M.F., Brielmann, R.M., Pedersen, J.S., and Morimoto, R.I. (2015). Investigating the spreading and toxicity of prion-like proteins using the metazoan model organism C. elegans. J. Vis. Exp. *95*, 52321.
61. Jensen, M.M., Jørgensen, J.T., Binderup, T., and Kjaer, A. (2008). Tumor volume in subcutaneous mouse xenografts measured by microCT is more accurate and reproducible than determined by 18F-FDG-microPET or external caliper. BMC Med. Imaging *8*, 16. https://doi.org/10.1186/1471-2342-8-16.
62. Aston, W.J., Hope, D.E., Nowak, A.K., Robinson, B.W., Lake, R.A., and Lesterhuis, W.J. (2017). A systematic investigation of the maximum tolerated dose of cytotoxic chemotherapy with and without supportive care in mice. BMC Cancer *17*, 684. https://doi.org/10.1186/s12885-017-3677-7.

Please cite this article in press as: Goto et al., Microendoscopy for periodic intravital end-to-end tumor imaging of cancer cells, Cell Reports Methods (2025), https://doi.org/10.1016/j.crmeth.2025.101056

CellPress
OPEN ACCESS

STAR★METHODS

KEY RESOURCES TABLE

REAGENT or RESOURCE	SOURCE	IDENTIFIER
Chemicals, peptides, and recombinant proteins		
Doxorubicin	Sigma-Aldrich	D1515; CAS: 25316-40-9
Bleomycin	Sigma-Aldrich	BP97; CAS: 19041-93-4
Pazopanib	Sigma-Aldrich	SML3076; CAS: 1149669-28-2
Sodium valproate	FUJIFILM Wako Pure Chemical Corporation	193-18352; CAS: 1069-66-5
DyLight 649 Lycopersicon esculentum (Tomato) lectin	Vector Laboratories	DL-1178
Experimental models: Cell lines		
HT1080/Fucci(SA)5 (clone #2)	RIKEN BioResource Research Center (BRC)	RCB 4698
C6	RIKEN BRC	RCB2854
Experimental models: Organisms/strains		
BALB/c (nu/nu) mice	CLEA Japan	BALB/cAJcl-nu/nu
Software and algorithms		
Pseudo-tomographic image synthesis program	This paper	https://osf.io/8345y/files/osfstorage?view_only=4d6af5e5bc054582a7ad369147e62e19 and https://doi.org/10.6084/m9.figshare.29035784
NIH ImageJ Fiji	Schindelin, J. et al.[59]	https://fiji.sc/
wrMTrck plugin	Nussbaum-Krammer, C. I. et al.[60]	https://www.phage.dk/plugins/wrmtrck.html
Other		
Optical fiber bundle	SUMITA OPTICAL GLASS, Inc.	HDIG
Optical fiber bundle	Fujikura	FIGH-10-350S
475 nm laser light source	Coherent	OBIS 473-75 LX
561 nm laser light source	Coherent	OBIS 561-50 LS
638 nm laser light source	CiviLasers	180 mW Red Semiconductor Laser system Solid state laser
Photomultipliers	Hamamatsu Photonics	R3896
ORIEL Dual Controller	Newport Corporation	Model 18009
Nonstandard analog framegrabber	Matrox	Solios eA
Dichroic mirror	IDEX Health&Science	Semrock Di01-R488/561
Dichroic mirror	IDEX Health&Science	Semrock FF561-Di01
Emission filter	IDEX Health&Science	Semrock FF01-525/32
Emission filter	IDEX Health&Science	Semrock FF01-600/35

EXPERIMENTAL MODEL AND STUDY PARTICIPANT DETAILS

Cell lines

For the generation of HT1080 human fibrosarcoma cells (ATCC, VA, USA) and C6 rat glioma cells (RIKEN BRC, Ibaragi, Japan) stably expressing tFucci(SA)5, the PiggyBac transposon system was employed.[26] The pPBbsr-based tFucci(SA)5 and pCMV-mPBase (neo-) encoding the *piggyBac* transposase were cotransfected into HT1080 cells or C6 using Lipofectamine 3000 or PEI MAX, respectively. The transfected cells were selected using blasticidin S (InvivoGen, CA, USA) (50 μg/mL for 3 days and subsequently 10 μg/mL for 7–10 days). tFucci-expressing single cell clones were further isolated by limited dilution.

Please cite this article in press as: Goto et al., Microendoscopy for periodic intravital end-to-end tumor imaging of cancer cells, Cell Reports Methods (2025), https://doi.org/10.1016/j.crmeth.2025.101056

Tumor xenograft models

Briefly, 4-week-old BALB/c (nu/nu) male mice (CLEA Japan, Inc., Tokyo, Japan) were used. All experimental protocols were approved by the Ethics Committee on Animal Care and Use of the RIKEN Center for Biosystems Dynamics Research (MAH 21-17-15) and performed in accordance with the Principles of Laboratory Animal Care. Animal care and use complied with the ARRIVE 2.0 guidelines. Mice were housed (2–3 animals in each cage) at a constant temperature (22°C–23°C) and humidity (50–60%) and were maintained under a 12 h light/dark cycle (lights off at 8:00 p.m.) with free access to food and water.

For the subcutaneous injection of tumor cells, mice were anesthetized with isoflurane (Pfizer, Groton, CT, USA) and then injected with 1.0–2.0 $\times$ 10^6 HT1080/Fucci(SA)5 cells in a 2:1 mixture of Hank's balanced salt solution and Matrigel Growth Factor Reduced Basement Membrane Matrix (Corning, Inc., Corning, NY, USA). Tumor volume was measured twice per week, and tumor size was calculated using the following formula[61]:

$$\text{Tumor size} = \text{length} \times \text{width}^2 / 2$$

For the brain ventricular injection of tumor cells, mice were anesthetized with isoflurane (Pfizer), and a head was fixed with a stereotaxic instrument (Narishige, Tokyo, Japan). The cannula was stereotaxically positioned in the left lateral ventricle after the skull was carefully removed. Next, 1.0 $\times$ 106 C6/Fucci(SA)5 cells in 5 μL of Hank's balanced salt solution were injected into the lateral ventricle. After closing the incision, penicillin G potassium (6000 U/day, Meiji Seika Pharma Co., Ltd., Tokyo, Japan) was injected intramuscularly for infection control.

METHOD DETAILS

Cell culture

HT1080 cells were cultured in Dulbecco's modified Eagle's medium (Nacalai Tesque, Kyoto, Japan) supplemented with 10% fetal bovine serum (FBS) (BIOSERA, Nuaille, France), 100 μg/mL penicillin (Nacalai Tesque), and 100 U/mL streptomycin (Nacalai Tesque) in an atmosphere containing 5% CO_2 at 37°C C6 cells were cultured in Roswell Park Memorial institute medium-1640 (Nacalai Tesque) supplemented with 10% FBS (BIOSERA), 100 μg/mL penicillin (Nacalai Tesque), and 100 U/mL streptomycin (Nacalai Tesque) in an atmosphere containing 5% CO_2 at 37°C.

Animal study

After tumors had reached a median size of 180–230 mm^3, the mice were divided into groups of eight animals based on similar median tumor sizes. Mice were injected with saline (vehicle; intraperitoneally), doxorubicin (DXR; 3.8 mg/kg; intravenously) (Sigma-Aldrich, St. Louis, MO, USA), or bleomycin (BLM; 20 mg/kg; intraperitoneally) (Sigma-Aldrich) every 2 days for 8 days. Furthermore, a mixture of pazopanib (PAZ; 25 mg/kg) (Sigma-Aldrich) and sodium valproate (Val; 50 mg/mL) (FUJIFILM Wako Pure Chemical Corporation, Osaka, Japan) was administered via oral gavage. The dosage of these anticancer drugs was determined based on previous *in vivo* studies.[31,62]

In vivo microendoscopic imaging

In vivo microendoscopic imaging was performed as previously described.[21–23,27] Fluorescence signals were detected using a fiber bundle (350 μm in diameter, high-definition image guide; HDIG, SUMITA OPTICAL GLASS, Inc., Saitama, Japan; or FIGH-10-350S, Fujikura, Tokyo, Japan). For tumor insertion, one tip of the bundle was placed in a 22G needle and polished at a 60° angle (Figure 1). The other end was flat and scanned using a custom-built laser scanning microscope equipped with a 475 nm laser light source (OBIS 473-75 LX, Coherent, Inc., CA, USA), 561 nm laser light source (OBIS 561-50 LS, Coherent, Inc.), 638 nm laser light source (638 nm 180 mW Red Semiconductor Laser, CiviLasers, China), and photomultipliers (R3896, Hamamatsu Photonics, Shizuoka, Japan). For confocal microscopy, the following dichroic mirrors and filters were used: Semrock Di01-R488/561 for excitation laser/emitted fluorescence, Semrock FF561-Di01 for two-color separation, and Semrock FF01-525/32 and FF01-600/35 as emission filters. Fluorescence signals were digitized using a nonstandard analog framegrabber (Solios eA, Matrox, Canada), and the data were stored on a PC using a custom-written Windows program (Neuro Programming Research, Osaka, Japan). The resolution of each image was set to 1200 (H) $\times$ 1000 (V) pixels. The frame rate depends on the number of scanning vertical lines; here, the frame rate was 7.5 fps owing to the acquisition of line numbers for image resolution. To confirm the spatial resolution and detection of multiple fluorescence signals, 1 μm (Ex: 485 nm, Em: 510 nm) (42-01-103, Micromod Partikeltechnologie GmbH, Rostock-Wamemunde, Germany), 2 μm (Ex: 660 nm, Em: 700 nm) (FP-2070-2, Spherotech, Inc., IL, USA), 5 μm (Ex: 569 nm, Em: 585 nm) (40-01-503, Micromod Partikeltechnologie GmbH), or 10 μm (Ex: 485 nm, Em: 510 nm) (42-01-104, Micromod Partikeltechnologie GmbH) fluorescence beads embedded in agarose gel were used.

HT1080/Fucci(SA)5 tumor-bearing mice were anesthetized with isoflurane. The tumor was held with a stereotaxic instrument (Narishige), and an optical fiber bundle was automatically inserted at a rate of 0.069 mm/s using the ORIEL Dual Controller Model 18009 (Newport Corporation, Irvine, CA, USA). During insertion, endoscopic images were continuously recorded. After recording, the optical fiber bundle was removed from the tumor, and the stab wound was disinfected with a povidone-iodine 7.5% w/w surgical scrub (Meiji Seika Pharma Co., Ltd., Tokyo, Japan). In some cases, animal death or lack of tumor solidity due to cachexia or anticancer drug

treatment interrupted periodic endoscopic imaging. C6/Fucci(SA)5 glioma model mice were anesthetized with isoflurane and a head was fixed with a stereotaxic instrument (Narishige). After exposing the brain, an optical fiber was inserted, and endoscopic imaging was performed in accordance with the procedure described above.

For vascular endoscopic imaging, HT1080/Fucci(SA)5 tumor-bearing mice were intravenously injected with DyLight 649 *Lycopersicon esculentum* (Tomato) lectin (5.0 mg/kg) (Vector Laboratories, Inc., CA, USA) before being anesthetized with isoflurane.

Image processing

The fluorescence intensity, size, and number of cells in the endoscopic images were analyzed using a cell tracking macro developed by NIH ImageJ Fiji.[59] For the cell tracking analysis, the background value was subtracted from the value of the averaged stacked images. A running Z-projector plugin was used to increase the signal/noise ratio in the subtracted images. The images were then rotated depending on the flow of cells and resized so that the ratio between the long and short axes of the elliptic fits of cells became close to that obtained using conventional confocal microscopic images. The contrast of the images was determined based on a histogram of stacked images. Threshold levels were determined using an autothreshold plugin. Small noises in the processed images were removed using the despeckle filter. Cell tracking was performed using the wrMTrck plugin.[60] The S/G2/M cell ratio was calculated as the ratio of tracked S/G2/M cells to the total number of cells (S/G2/M and G1/G0 cells). Nuclear sizes were obtained by running the wrMTrck plugin.

Pseudo-tomographic image synthesis

All steps in the synthesis program were built in C++. The input optical fiber imaging movie was subjected to a Laplacian of Gaussian filter. Background subtraction and binarization were performed for each channel. Objects were detected to obtain the desired size and velocity. The objects were tracked, and bounding boxes were drawn using a tracking program in OpenCV. The vectors of each tracking object were obtained at the same times as those of the tracking phase and averaged as an integrated vector. In addition, the tracking images collected from each frame were averaged, and the aspect ratios of the averaged images were then corrected. Virtual (constant vector) and actual fiber tracts were generated from the desired and integrated vectors, respectively. The corrected images were arranged for coordination based on the initial tracking points located in each fiber tract. In cases where the tissue contained necrotic areas, the constant vector was used to obtain the pseudo-tomographic image.

Histological analysis

HT1080/Fucci(SA)5 tumor-bearing mice were deeply anesthetized with isoflurane. The tumors were collected, postfixed overnight with 4% paraformaldehyde (MilliporeSigma, Burlington, MA, USA) in 10 mM phosphate-buffered saline at 4°C, and sequentially immersed in 15% and 30% (w/v) sucrose solutions. Tumor sections (30 μm-thick) were prepared using a cryostat (Microm HM 560, Microedge Instrument, Inc., BC, Canada). The tumor sections were mounted with a solution containing Hoechst (5 mg/mL; Dojindo Laboratories, Tokyo, Japan) and observed under a confocal laser microscope (Digital Eclipse C1; Nikon, Tokyo, Japan). For conventional hematoxylin-eosin staining, the tumor sections were stained by Weigert's Iron Hematoxylin (FUJIFILM Wako Pure Chemical Corporation) and diluted pure eosin solutions (Muto Pure Chemicals Co., Ltd., Tokyo, Japan). The hematoxylin-eosin staining tumors were mounted with Entellan new (Merck Millipore, MA, USA) and observed under a phase contrast microscope.

QUANTIFICATION AND STATISTICAL ANALYSIS

All data are presented as the mean ± standard error of mean (SEM) of representative experiments unless otherwise stated. Each experiment was repeated at least thrice and involved at least triplicate measurements. Statistical significance was calculated using Student's t *t*-test or one-way analysis of variance (ANOVA), followed by the Tukey–Kramer test. Statistical significance was set at a p value <0.05.